Title

Coupling between slow waves and sharp-wave ripples engages distributed neural activity during sleep in humans.

Authors

Skelin, Ivan
Zhang, Haoxin
Zheng, Jie
et al.

Peer reviewed

Coupling between slow waves and sharp-wave ripples engages distributed neural activity during sleep in humans

Ivan Skelin[a,b,1], Haoxin Zhang[a,c], Jie Zheng[c], Shiting Ma[a], Bryce A. Mander[d], Olivia Kim McManus[e,f], Sumeet Vadera[g], Robert T. Knight[h,i], Bruce L. McNaughton[b,j], and Jack J. Lin[a,c,1]

[a]Department of Neurology, University of California, Irvine, CA 92603; [b]Department of Neuroscience, University of Lethbridge, Lethbridge, AB T1K 3M4, Canada; [c]Department of Biomedical Engineering, University of California, Irvine, CA 92603; [d]Department of Psychiatry and Human Behavior, University of California, Irvine, CA 92603; [e]Department of Neurosciences, University of California, San Diego, CA 92093; [f]Division of Neurology, Rady Children's Hospital, San Diego, CA 92123; [g]Department of Neurological Surgery, University of California, Irvine, CA 92603; [h]Department of Psychology, University of California, Berkeley, CA 94720; [i]Helen Wills Neuroscience Institute, University of California, Berkeley, CA 94720; and [j]Department of Neurobiology and Behavior, University of California, Irvine, CA 92603

Hippocampal-dependent memory consolidation during sleep is hypothesized to depend on the synchronization of distributed neuronal ensembles, organized by the hippocampal sharp-wave ripples (SWRs, 80 to 150 Hz), subcortical/cortical slow-wave activity (SWA, 0.5 to 4 Hz), and sleep spindles (SP, 7 to 15 Hz). However, the precise role of these interactions in synchronizing subcortical/cortical neuronal activity is unclear. Here, we leverage intracranial electrophysiological recordings from the human hippocampus, amygdala, and temporal and frontal cortices to examine activity modulation and cross-regional coordination during SWRs. Hippocampal SWRs are associated with widespread modulation of high-frequency activity (HFA, 70 to 200 Hz), a measure of local neuronal activation. This peri-SWR HFA modulation is predicted by the coupling between hippocampal SWRs and local subcortical/cortical SWA or SP. Finally, local cortical SWA phase offsets and SWR amplitudes predicted functional connectivity between the frontal and temporal cortex during individual SWRs. These findings suggest a selection mechanism wherein hippocampal SWR and cortical slow-wave synchronization governs the transient engagement of distributed neuronal populations supporting hippocampal-dependent memory consolidation.

sharp wave/ripples | slow waves | spindles | sleep | human brain

Memory consolidation involves the transformation of newly encoded representations into long-term memory (1–3). During non-rapid eye movement (NREM) sleep, hippocampal representations of recent experiences are reactivated (4, 5), along with transient synchronization of distributed subcortical and cortical neuronal populations (6, 7). It is hypothesized that the oscillatory synchrony facilitates connections between the neuronal ensembles, stabilizing memory representations (8). The selection and synchronization of distant neuronal populations that participate in hippocampal-dependent memory consolidation are proposed to depend on the interaction between hippocampal sharp-wave ripples (SWRs, 80 to 150 Hz), traveling subcortical/cortical slow-wave activity (SWA, 0.5 to 4 Hz), and sleep spindles (SP, 7 to 15Hz), but the underlying mechanisms subserving this network engagement are unclear. Here, we investigated how hippocampal SWRs and subcortical/cortical slow waves and spindles coordinate distributed neuronal populations during memory consolidation in NREM sleep.

Hippocampal SWRs are transient local field potential oscillations (20 to 100 ms; 80 to 150 Hz in humans) implicated in planning, memory retrieval, and memory consolidation (9). Several lines of evidence highlight the role of SWRs in sleep-dependent memory consolidation. First, memory reactivation in the hippocampus, cortical, and subcortical structures peaks during SWRs (4–7, 10, 11). Second, hippocampal–subcortical/cortical functional connectivity,

the prerequisite for binding of anatomically distributed reactivated memory traces is enhanced around SWRs (7, 12–15). Finally, SWR suppression interferes with, while prolongation of SWR duration improves hippocampal-dependent memory consolidation (16, 17).

While research converges on the notion that SWR output modulates neuronal activity across brain regions during NREM sleep, SWR events are temporally biased by phases of SWA and SWA-nested SP (18–20). SWA and SP are present in cortical and subcortical structures (21, 22), originate in frontal areas, and traverse in an orderly succession to temporal lobes and subcortical structures, including the hippocampus (18, 22–24). Indeed, SWA synchrony increases following learning, and the reduction of SWA synchrony is correlated with memory impairment (25). Finally, although SWA is ubiquitous, individual SWA trajectories are usually limited to a subset of cortical/subcortical areas, with ~80% of these events detected in less than half of recorded locations in humans (22). Therefore, each SWR-associated SWA event could recruit and index a unique sequence of cortical and subcortical populations.

Significance

Hippocampal sharp wave/ripples (SWRs) are implicated in binding distributed subcortical/cortical neuronal populations during sleep, supporting hippocampal-dependent memory consolidation. We assessed the activation and functional interactions between distributed populations during SWRs using intracranial electrophysiological recordings from human epileptic patients. Consistent phase relation between the hippocampal SWRs and local subcortical/cortical slow-wave activity (SWA) or spindles was a strong predictor of local neuronal activation during SWRs. In addition, individual SWR amplitude and SWA phase difference between the cortical sites during SWRs predicted the functional coupling between the distant cortical populations. Our findings suggest the SWR–SWA coupling as a mechanism for selecting and organizing the distributed populations for participation in global memory consolidation.

In this study, we used the broadband high-frequency activity (HFA, 70 to 200 Hz) recorded from human intracranial electrodes as a metric of subcortical/cortical activity. HFA is an indirect measure of multiunit spiking from the population surrounding the electrode contact (26), estimated in the range of several hundred thousand neurons. Consistent with the hypothesized role of SWR in synchronizing distributed memory traces, we found HFA power modulation during hippocampal SWR events in ∼30% of extra-hippocampal recording sites. Given the critical role of SWA in facilitating hippocampal-dependent memory consolidation (13) and their confinement to local regions (22), we hypothesize that interplay between SWA and SWRs organizes hippocampal–cortical and cortical–cortical interactions during SWR events. Indeed, we found a strong association between SWR phase locking to extrahippocampal SWA or SP and HFA modulation in the same recording site. Interestingly, while the SWR–SWA phase locking was present bilaterally, the SWR–SP phase locking was limited to the hemisphere of SWR origin. These findings suggest that coupling between the hippocampal SWRs and extrahippocampal SWA/SP drives the selection of cortical populations to participate in hippocampal–cortical communication. In addition, theoretical constructs of memory consolidation predict transient synchronization of neuronal populations in distant cortical regions during hippocampal SWRs. Based on the widespread presence of SWA during NREM sleep, SWA–SWR temporal coupling, and ability of SWA to synchronize large cortical areas, we hypothesized that the pairwise phase relation between the SWA in different cortical locations could predict the functional coupling between the local cortical populations during SWR windows. In support of the cooperative role of SWR and SWA in orchestrating cortical–cortical communication, we found that SWA phase alignments between two distant cortical sites predicted their neuronal population synchronization during individual SWR windows, manifested by temporal HFA power correlations. The amplitude of individual SWRs was another strong predictor of cortico–cortical coupling, while the combination of SWA phase difference and SWR amplitude outperformed the predictive accuracy of the phase difference or SWA amplitude individually. These results imply a recruitment mechanism by which interplay of SWA and SWRs provides communication windows for long-range interactions between distributed neuronal populations, critical for hippocampal-dependent memory consolidation.

Results

Sleep Staging and SWR Detection. We recorded overnight sleep intracranial electroencephalograms (iEEGs) in 12 subjects (573 ± 18 min, mean ± SEM; range 480 to 725) simultaneously from the frontal lobe (including the orbitofrontal, medial prefrontal, dorsomedial, and cingulate cortices), temporal lobe (including the insula, entorhinal, parahippocampal, inferior, medial, and superior temporal cortices), amygdala (including the basolateral, lateral, and centromedial amygdala), and hippocampus (Fig. 1 A–C). The localization of the depth electrodes was determined based on coregistered pre- and postimplantation MRI, as well as registration to a high-resolution atlas. A trained researcher (B.A.M.) performed sleep staging guided by standard criteria (27) (Fig. 1D) using polysomnography data collected from surface electrodes (i.e., electroencephalography, electrooculography, and electromyography). On average, subjects spent 287 ± 44 min (range 115 to 405 min) in NREM sleep, which represented 49.9 ± 4.1% of overnight sleep recording durations. The anti-epileptic medication was tapered off for diagnostic purposes, but the sleep architecture parameters were within the range reported in healthy subjects (28) (*SI Appendix*, Table S2). We used depth electrodes implanted in the hippocampus to detect SWR events (*Methods*). Hippocampal iEEGs were bandpass filtered in the SWR frequency range (80 to 150 Hz), rectified, and transformed to z-scores (Fig. 1E). Events that exceeded five SDs from the mean amplitude and were beyond a 1-s window of the nearest interictal epileptic discharges (IEDs)

(*SI Appendix*, Fig. S1 A and B) were classified as SWRs. The peak of the rectified SWR range envelope was considered the SWR occurrence time. The morphology of grand-average SWR (n = 12 subjects; 44,965 SWRs, Fig. 1E) and the SWR densities (number of events per minute, 5.1 ± 1.7, grand-average ± SEM, *SI Appendix*, Table S3) were consistent across subjects and in line with previous reports from humans and nonhuman primates (19, 29–31)

Hippocampal SWRs Modulate Subcortical and Cortical High-Frequency Activity. Functional MRI studies show a widespread peri-SWR activity modulation (32), but the precise timing and anatomical distribution of the neuronal activity is unclear. Therefore, we leveraged millisecond temporal resolutions and broad anatomical coverage of intracranial electrophysiological recordings to measure HFA power (a proxy of neuronal population activity) during SWR windows (±250 ms, relative to SWR peak). We paired each hippocampal recording site containing a minimum of 100 SWRs/overnight recording session with simultaneously recorded extrahippocampal recording sites and operationally defined the paired extrahippocampal recording sites as target sites (n = 1,308, 625 ipsilateral, and 683 contralateral to SWR location; Fig. 2A). All of the electrodes used in the analysis were localized in gray matter (*Methods*). Based on the presence or absence of significant peri-SWR HFA modulation (*Methods*), target sites were classified as either HFA+ or HFA−. We found significant peri-SWR HFA power modulation in 36.7 ± 9.1% of target sites. Peri-SWR HFA modulations were classified as either 1) positive (increased HFA), 2) negative (decreased HFA), or 3) mixed (both periods of increased and decreased HFA; Fig. 2 B and C). Positive modulations were the most common modulation class (78.0 ± 7.1% of HFA-modulated target sites), followed by mixed modulations (18.5 ± 6.2%) and negative modulations (3.5 ± 1.8%). The percentage of peri-SWR HFA–modulated subcortical/cortical target sites was significantly higher when SWRs originated from the same (ipsilateral) hemisphere versus SWRs arising from the contralateral hemisphere (ipsilateral 50.9 ± 8.5% versus contralateral 7.5 ± 3.7%; linear mixed-effects model, $t(1,306) = -10.69, P < 10^{-10}$, *SI Appendix*, Fig. S2A). The highest percentage of modulated sites were in the amygdala (88.9 ± 11.1% ipsilateral and 23.2 ± 15.5% contralateral to SWR), followed by the temporal (67.8 ± 8.6% ipsilateral and 10.8 ± 6.5% contralateral) and the frontal cortex (9.8 ± 4.4% ipsilateral and 6.2 ± 3.7% contralateral; Fig. 2C and *SI Appendix*, Fig. S2B). Detailed statistical comparisons of regional and hemispheric peri-SWR HFA modulation are shown in *SI Appendix*, Table S4. Overall, these findings suggest an anatomically specific engagement of neuronal populations during SWR windows.

SWR Phase Locking with Subcortical/Cortical SWA and SP Is Associated with Local Activity Modulation. If SWA and SP rhythmically modulate neuronal excitability (21, 22), we hypothesized that the phase locking between hippocampal SWRs and SWA or SP at individual subcortical/cortical target sites would predict local HFA modulation. For each target site, the phase locking between hippocampal SWRs and local SWA or SP is considered significant if the real phase-locking value (PLV) (33) exceeded 98% of null distribution (*Methods*). PLV null distribution was created by randomly jittering the individual SWR times within a ±1-s window for 1,000 times and calculating the PLV of each jittered distribution. First, we found a higher percentage of target sites with SWR–SWA or SWR–SP phase locking in the ipsilateral, compared to contralateral hemisphere, relative to the SWR location (SWA: 38.0 ± 6.0% versus 6.1 ± 2.1%, linear mixed-effects model, $t(1,306) = -13.5$, $P < 10^{-10}$; SP: 30.8 ± 7.9% versus 2.6 ± 0.9%, linear mixed-effects model, $t(1,306) = -14.3, P < 10^{-10}$; *SI Appendix*, Fig. S3A). Second, the percentage of SWR–SWA or SWR–SP phase locking was significantly higher for HFA+, relative to HFA− sites (Fig. 3B and *SI Appendix*, Fig. S3 A and D; SWA: ipsilateral HFA+ = 61.4 ± 7.6% versus HFA− = 16.2 ± 3.5%, $t(623) = 17.0, P < 10^{-10}$;
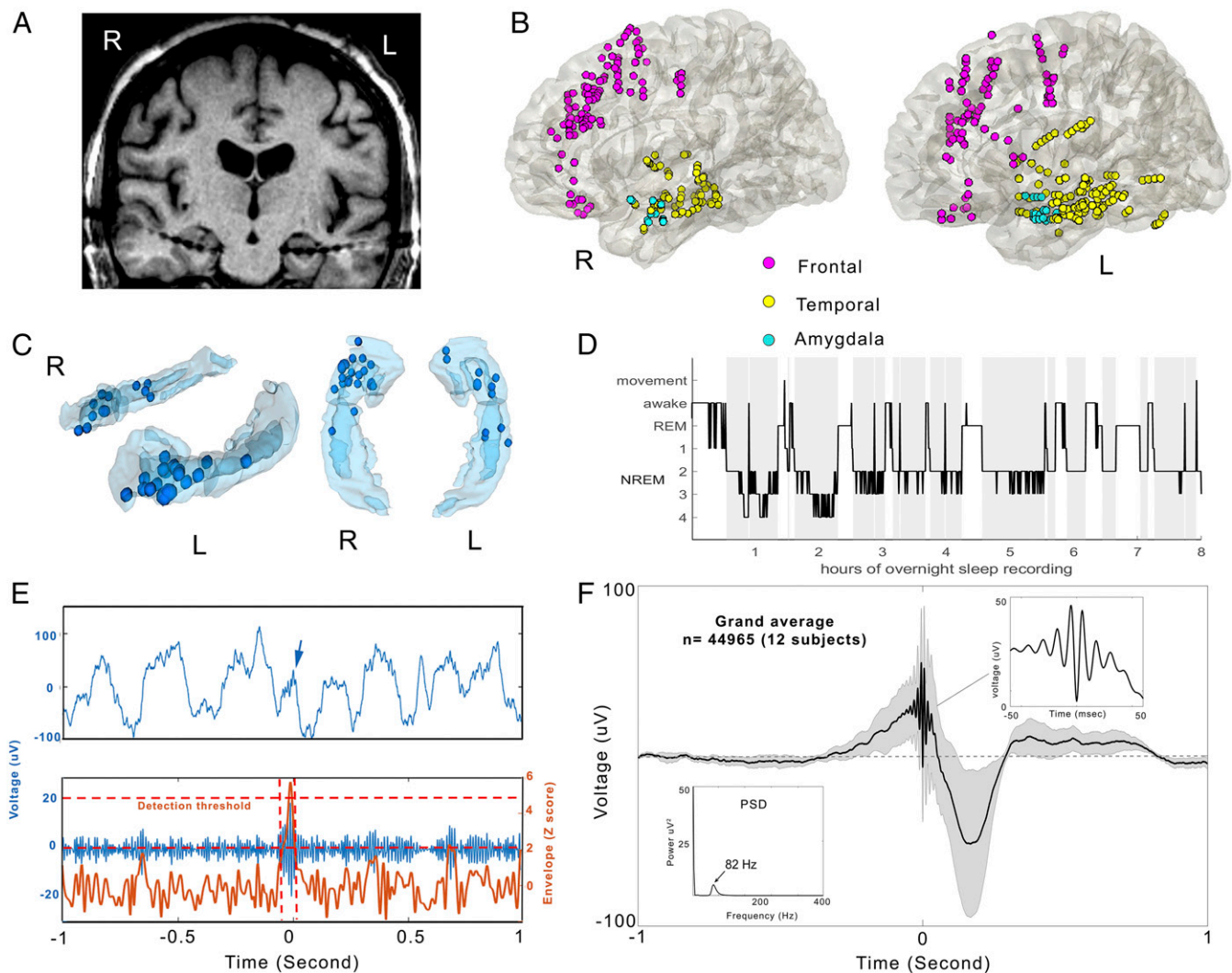
Fig. 1. Recording locations, sleep staging, and SWR detection. (*A*) Coronal MRI image from an example subject, showing the depth electrodes targeting the hippocampus bilaterally. The thicker areas along the electrode shafts represent the individual recording contacts. (*B*) Anatomical distribution of extra-hippocampal recording locations (amygdala—cyan, n = 36; temporal cortex—yellow, n = 180; frontal cortex—magenta, n = 189; medial views of the right (R) and left (L) hemispheres. Regional electrode distributions across individual subjects are shown in the *SI Appendix*, Table S1. (*C*) Hippocampal electrode localizations (n = 32) from all the subjects, shown on a three-dimensional hippocampus model. The blue dots indicate the individual electrode locations in the left (L) or right (R) hippocampus. (*D*) Overnight sleep hypnogram from an example dataset. The NREM stages 2 to 4 were used in the analysis (gray). (*E*) Example of detected SWR and illustration of the detection algorithm. *Top*: raw iEEG trace around the SWR (arrow). *Bottom*: blue—the iEEG trace shown in the top plot, bandpass filtered in the SWR range (80 to 150 Hz). Orange—z-scored envelope of the filtered trace. SWR detection was based on the coincidence of two criteria: 1) SWR envelope peak crossing the mean + 5 SD (upper threshold, top dashed orange line) and 2) SWR envelope around the candidate upper threshold crossing exceeding mean + 2 SD for 20 to 100 ms (lower threshold, bottom dashed orange line). (*F*) Grand-average SWR-centered raw iEEG (mean ± SEM; n = 12 subjects). Time 0 corresponds to SWR peak. (*Top Right Inset*) Several oscillatory cycles around the grand-average SWR peak reflect the oscillatory nature of detected SWR events, lasting several tens of ms. (*Bottom Left Inset*) Power spectral density (PSD) averaged across all detected SWRs. The unimodal peak (82 Hz) suggests the lack of contamination with epileptic activity, which is typically reflected as an additional PSD peak in >200-Hz range (30).

contralateral HFA+ = 24.6 ± 7.1% versus HFA− = 4.4 ± 1.5%, linear mixed-effects model, $t(681) = 9.2$, $P < 10^{-10}$; SP: ipsilateral HFA+ = 54.2 ± 9.3%, HFA− = 7.1 ± 2.3%, $t(623) = 17.4$, $P < 10^{-10}$), except for the SWR phase locking to SP in contralateral hemisphere, which was very rare (HFA+ = 7.1 ± 6.6%, HFA− = 2.7 ± 0.9%, $t(681) = −0.53$, $P = 0.60$, *SI Appendix*, Fig. S3A). Further, a significantly higher percentage of SWR–SWA phase locking in HFA+ relative to HFA− target sites was present in all recorded brain regions (*SI Appendix*, Fig. S3C and Table S5, all Ps < 10^{-3}). Similarly, the percentage of SWR–SP phase locking was significantly higher among the HFA+, relative to HFA− target sites in all the ipsilateral recorded regions (*SI Appendix*, Fig. S3C and Table S6, all Ps < 10^{-4}). Finally, the association between the SWR–SWA or SP phase locking and local peri-SWR HFA

modulation is reflected by significantly higher PLV at HFA+, relative to HFA− target sites (SWR–SWA PLV, Fig. 3C: HFA+ 0.22 ± 0.05, HFA− 0.07 ± 0.01, linear mixed-effect model, $t(1,306) = 19.0$, $P < 10^{-10}$; SWR–SP PLV, *SI Appendix*, Fig. S3E: HFA+ 0.19 ± 0.05, HFA− 0.06 ± 0.01, linear mixed-effect model, $t(1,306) = 17.3$, $P < 10^{-10}$).

The anatomical selectivity of SWR–SWA and SWR–SP phase locking is not attributable to SWA or SP amplitude differences, as this parameter is not different between target sites with and without significant SWR–SWA (*SI Appendix*, Fig. S3B; linear mixed-effects model, $t(1,306) = 1.2$, $P = 0.23$) or SWR–SP phase-locking (*SI Appendix*, Fig. S3B; linear mixed-effects model, $t(1306) = 1.0$, $P = 0.31$. In summary, these findings indicate that the phase locking between hippocampal SWRs and target site
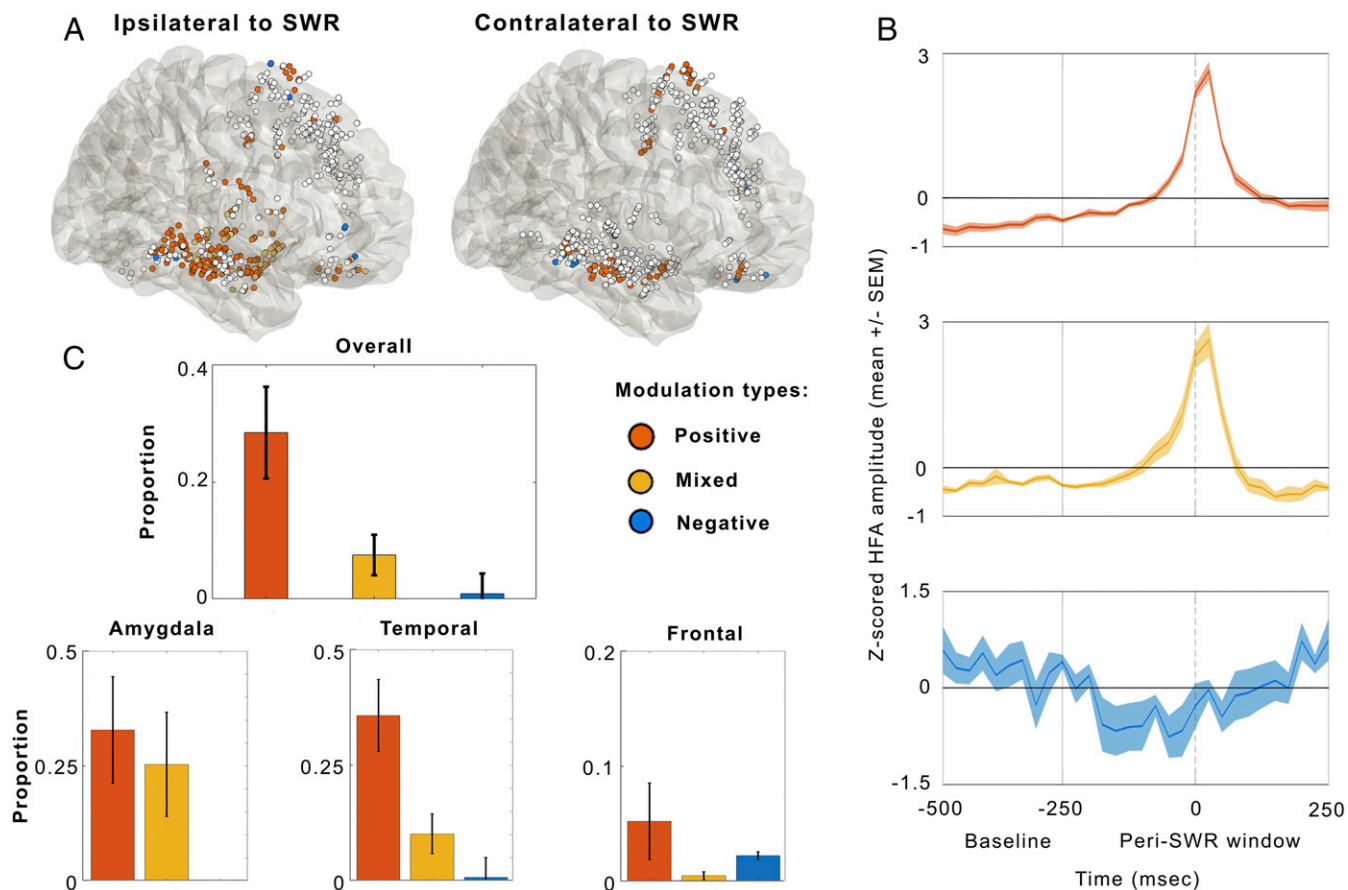
Skelin et al.
Coupling between slow waves and sharp-wave ripples engages distributed neural activity
during sleep in humans

PNAS | 3 of 10
https://doi.org/10.1073/pnas.2012075118

Fig. 2. HFA modulation around SWRs. (*A*) Anatomical distributions of peri-SWR HFA modulation ipsilateral (*Left*) and contralateral (*Right*) to SWR location. Orange, positive modulation; blue, negative modulation; ocher, mixed modulation; and white, no modulation (1,308 target sites, 625 ipsilateral and 683 contralateral to SWR location). The target sites are defined as extrahippocampal recording locations. When SWRs are recorded from multiple hippocampal channels in the same subject, locations of target sites are minimally jittered for visualization purposes. The most common significant peri-SWR HFA modulations are positive modulations ipsilateral to SWR location in temporal and amygdala sites. See Movie S1 for the temporal dynamics of peri-SWR HFA modulation. (*B*) *z*-scored peri-SWR HFA time courses (grand average ± SEM) from all the target sites showing a given modulation type (positive modulation, top; mixed modulation, middle; negative modulation, bottom). The thick vertical line denotes the boundary between baseline (−500 to −250 ms, relative to SWR peak time) and peri-SWR window (±250 ms around SWR peak time). SWR peak time is denoted by the dashed vertical line. (*C*) Percentages of significant peri-SWR HFA modulation overall (top chart) and at the regional level (bottom charts; grand average ± SEM). Orange, positive modulation; blue, negative modulation; ocher, mixed modulation; and white, no modulation.

SWA or SP is a potential mechanism for selecting neuronal populations to participate in widespread synchronous activity during SWRs.

SWA Phase Difference and SWR Amplitude Predict Cortico–Cortical Coupling. As demonstrated by simultaneous recordings from multiple locations in the monkey visual cortex, neuronal population locking to specific phases of local gamma oscillations determines their functional coupling (34). Similarly, we hypothesized that the HFA locking to oscillatory phases during SWR windows determines the pairwise HFA coupling between populations across the subcortical/cortical regions, organizing transiently connected distributed neuronal coalitions (35). HFA coupling is defined as the temporal correlation between the HFA analytic amplitude time courses at different target sites. To test this hypothesis, we first quantified the target-site pairwise HFA coupling during SWR windows using two different methods. The generalized linear model (GLM) and Pearson correlation. We analyzed the interregional functional coupling in four subjects with simultaneously recorded target sites in the amygdala, temporal, and frontal cortices, showing both significant peri-SWR HFA modulation and significant SWR–SWA phase locking. A total of 49 frontal–temporal

target site pairs with 150,532 SWR events were used in the analysis (subject 1: 16 pairs, 76,762 SWR events; subject 2: 3 pairs, 3,414 SWR events; subject 3: 5 pairs, 10,816 SWR events; and subject 4: 25 pairs, 59,540 SWR events). In addition, we analyzed 117 amygdala–temporal target site pairs with 377,574 SWR events (subject 1: 44 pairs, 265,838 SWR events; subject 2: 31 pairs, 52,254 SWR events; subject 3: 8 pairs, 1,930 SWR events; subject 4: 34 pairs, 57,552 SWR events). The support-vector machine (SVM) linear model was trained to predict the presence of pairwise HFA coupling between the two target sites (determined relative to coupling null distribution, *Methods*) based on the local SWA phase differences during a given SWR event. The model was trained separately on individual subjects, avoiding the possibility that the results are biased by the subjects with larger number of data points. Following 100 training–testing iterations, we obtained the distribution of coupling prediction accuracies in each individual subject (Fig. 4). We first compared the performances of the models trained to predict coupling defined by two different metrics (GLM-derived β or Pearson correlation r). For both the frontal–temporal and amygdala–temporal target site pairs, prediction of β-based coupling was significantly better than the prediction of r-based coupling (Fig. 4*A*; frontal–temporal: β-coupling prediction accuracy = 66.9 ± 3.0%,
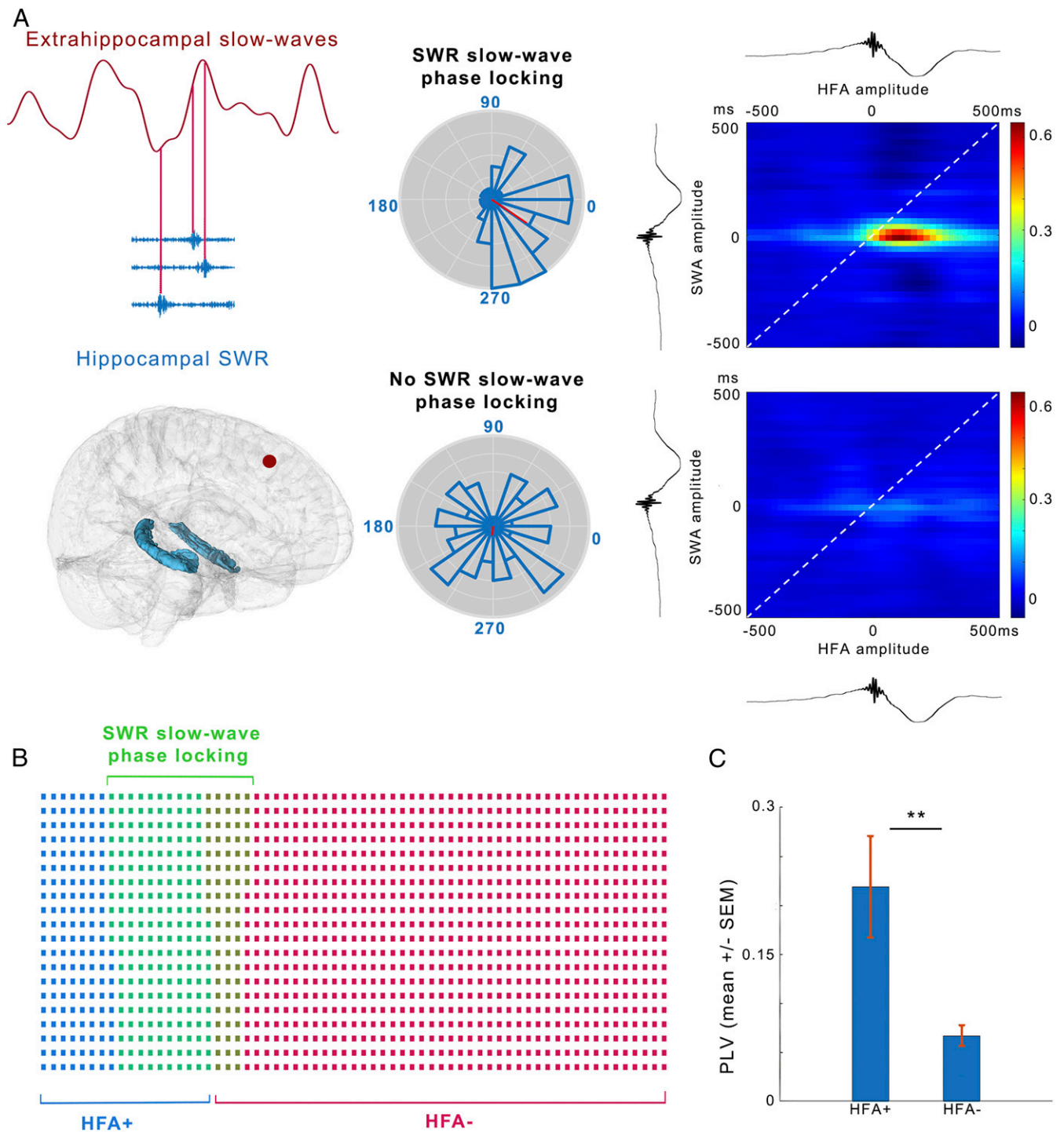
Fig. 3. SWR phase locking to subcortical/cortical SWA is associated with local peri-SWR HFA modulation. (*A*) Illustration of the SWR–SWA phase locking. Local SWA phases from an example extrahippocampal target site (maroon) corresponding to SWR peak times on simultaneously recorded hippocampal channel (blue) are used to construct the target site–specific circular distribution of SWA phases coinciding with hippocampal SWR peaks. The PLV significance was defined as the real PLV > 98% of null distribution. Depending on the PLV significance, the target sites are classified as showing SWR–SWA phase locking (SWR–SWA+) or no phase locking (SWR–SWA−). (*Middle*) Polar plots showing the distribution of SWA phases at SWR peak times for the example SWR–SWA+ (*Top*) and SWR-SWA- (*Bottom*) target sites. (*Right*) Joint peri-SWR time histogram of *z*-scored SWA and HFA amplitudes for SWA–SWR+ (*Top*, n = 11 subjects, grand average) and SWA–SWR target sites (*Bottom*, n = 12 subjects, grand average). SWA and HFA amplitudes increase around the SWR time, with a slightly delayed increase of HFA. This dynamic is observed selectively on target sites showing significant SWR–SWA phase locking. (*B*) Venn diagram showing the larger overlap between the target sites showing SWR–SWA phase locking (green) and HFA+ (blue), relative to HFA− (red) target sites. The individual target sites are represented as squares. (*C*) SWR–SWA PLV is significantly higher in target sites showing significant peri-SWR HFA modulation (HFA+) relative to target sites with no modulation (HFA−). Linear mixed-effect model; $t(1,306) = 19.0$, $P < 10^{-10}$.

Skelin et al.
Coupling between slow waves and sharp-wave ripples engages distributed neural activity
during sleep in humans

PNAS | 5 of 10
https://doi.org/10.1073/pnas.2012075118

NEUROSCIENCE

r-coupling prediction accuracy = 59.7 ± 2.6%; linear mixed-effects model, $t(798) = 22.0$, $P < 10^{-10}$; amygdala–temporal pairs: β-coupling prediction accuracy = 59.4 ± 2.6%, r-coupling prediction accuracy = 55.4 ± 2.0%; linear mixed-effects model, $t(798) = 13.5$, $P < 10^{-10}$). The better performance of models predicting β-coupling could be due to the ability of GLM to factor out the spurious contribution of common coupling to global activity. Based on this result, we focused the further analysis on the models predicting β-coupling as a likely more reliable estimate of functional connectivity. Next, we compared the performances of models predicting β-coupling of frontal–temporal pairs compared to amygdala–temporal pairs. Predictive accuracy was significantly higher for the frontal–temporal pairs, relative to amygdala–temporal pairs (Fig. 4B; frontal–temporal pairs: β-coupling prediction accuracy = 66.9 ± 3.0%, amygdala–temporal pairs: β-coupling prediction accuracy = 59.4 ± 2.6%; linear mixed-effects model, $t(798) = 26.0$, $P < 10^{-10}$). Thus, the pairwise local SWA phase differences between the two target sites are stronger predictors of pairwise HFA coupling in the frontal–temporal network compared to amygdala–temporal network. After establishing predictability of cortico–cortical coupling based on SWA phase differences at SWR time, it remained unclear if the SWRs are associated with this process, beyond the simple temporal coincidence. To answer this question, we trained a separate model to predict the frontal–temporal β-coupling based on the SWR amplitude. Predictability of β-coupling based on the SWR amplitude was above the chance level (Fig. 4C; 69.4 ± 2.6%). As the higher amplitude SWRs typically recruit larger hippocampal populations (36), the predictability of cortico–cortical coupling based on the SWR amplitude could suggest a widespread activation of cortical networks by the stronger hippocampal SWR output or the larger hippocampal recruitment during SWR based on the synchronized input from cortex. Finally, we tested if combining the SWA phase difference and SWR amplitude in a single model could improve the prediction accuracy beyond the level achieved by SWA phase difference or SWR amplitude as individual predictors. Indeed, the β-coupling prediction accuracy based on the combination of SWA phase difference and SWR amplitude was the highest among all the tested models (Fig. 4C; 71.8 ± 3.5%), showing a significantly better performance relative to both SWA phase difference (linear mixed-effects model; $t(798) = 14.2$, $P < 10^{-10}$) and SWR amplitude–based models ($t(798) = 8.6$, $P < 10^{-10}$).
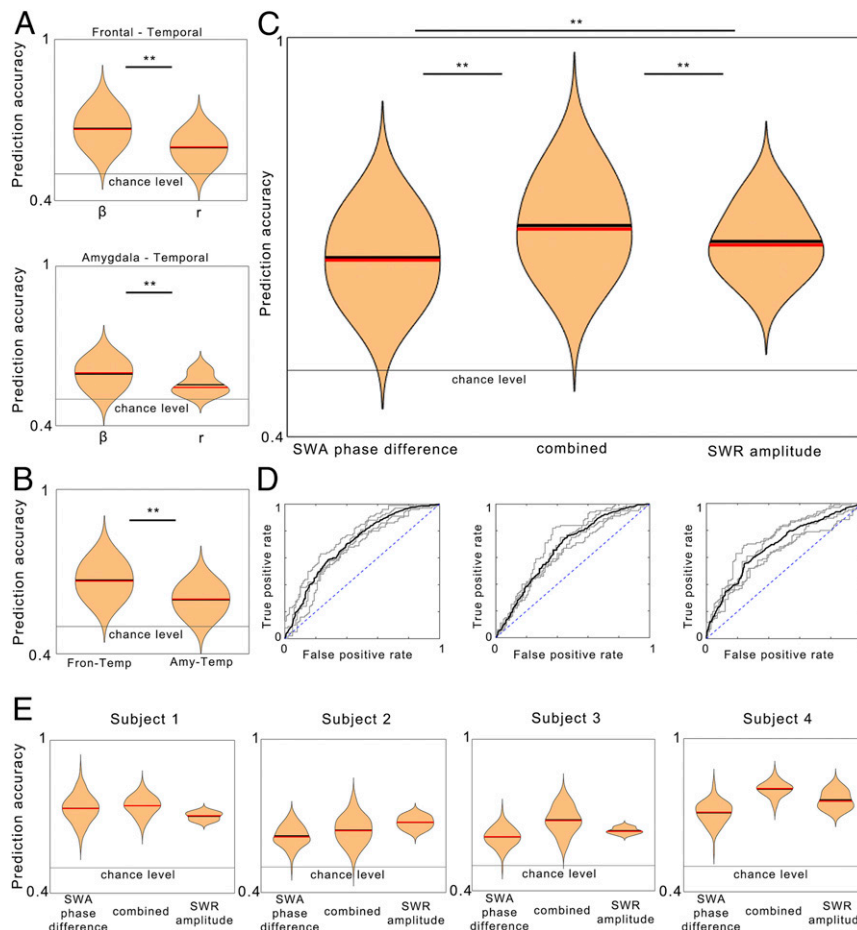

Fig. 4. SWA phase difference and SWR amplitude predict cortico–cortical coupling. (A) Coupling prediction accuracy based on SWA difference is significantly better when the GLM-derived β-coefficient is used as a coupling metric compared to Pearson r coefficient. This effect is present both for the frontal–temporal (linear mixed-effects model, $t(798) = 22.0$, $P < 10^{-10}$) and amygdala–temporal target site pairs ($t(798) = 13.5$, $P < 10^{-10}$). (B) GLM-β prediction accuracy based on SWA phase difference is significantly better for the frontal–temporal relative to amygdala–temporal pairs (linear mixed-effects model, $t(798) = 26.0$, $P < 10^{-10}$). (C) GLM-β coupling prediction accuracy for frontal–temporal pairs is above the chance level when the SWR amplitude is used as a predictor (69.4 ± 2.6%; chance level = 50%). In addition, combined prediction accuracy of SWR amplitude and SWA phase difference outperforms each individual predictor alone (linear mixed-effects model; SWA phase difference versus combined: $t(798) = 14.2$, $P < 10^{-10}$; SWR amplitude versus combined: $t(798) = 8.6$, $P < 10^{-10}$). (D) Receiver operating characteristic curves for the GLM-β coupling prediction accuracy based on SWA phase difference, SWR amplitude, and combination of those two predictors. (E) The model performances are consistent across all the analyzed subjects.

Discussion

These findings reveal widespread modulation of brain activity during hippocampal SWRs. Extensive literature has implicated SWRs as time windows of memory reactivation in the hippocampus and associated subcortical/cortical structures (9, 37). In addition, there is a strong correlation between peri-SWR activity modulation in a given location and phase-locking between hippocampal SWRs and local subcortical/cortical SWA and SP. Thus, SWR–SWA or SWR–SP phase locking may act as a mechanism for selecting distributed populations recruited simultaneously with hippocampal memory traces reactivated during SWRs. Finally, functional coupling between the pairs of sites in frontotemporal network during SWR windows is correlated with phase offsets between the local SWA as well as with SWR amplitude. This could underlie the formation of temporary neuronal coalitions around the SWRs, as predicted by memory consolidation theories (3, 35, 38).

Peri-SWR HFA Modulation. Most of the peri-SWR HFA modulations were positive, in line with the observations of widespread increase in cortical blood oxygen level–dependent signal and the higher probability of cortical gamma bursts during peri-SWR windows (29, 32). Mixed peri-SWR HFA modulations were mostly present in temporal lobe ipsilateral to SWR location, manifested as HFA increase around the SWR peak, followed by decrease 100 to 200 ms later (Fig. 2*B* and Movie S1). Peri-SWR HFA–negative modulations were of lower amplitude and most common in the frontal cortex (∼30% of modulations in that region; Fig. 2 *B* and *C*). The presence of both positively and negatively modulated peri-SWR HFA in frontal areas could reflect consistent co-occurrence of local up-to-down or down-to-up state transitions with SWRs. However, the low SWR density during cortical down states (7, 22) and the wider spatial synchronization of down states (22) would likely result in more widespread peri-SWR HFA–negative modulation than observed in the present data. Another possible interpretation of frontal peri-SWR HFA–negative modulations could be the recruitment of local inhibitory networks, similar to increased firing of inhibitory interneurons in deep layers of rodent prefrontal cortex during SWRs (39).

Peri-SWR HFA modulation is region and hemisphere dependent, with higher percentages ipsilateral to SWR location (*SI Appendix*, Fig. S2 *A–C* and Movie S1) as well as in the temporal lobe structures (amygdala and temporal cortex), where it reached >70 to 90% of target sites in the ipsilateral and 10 to 25% in the contralateral hemisphere. Interestingly, hemispheric differences were not present in the frontal cortex, where up to 10% of sites were modulated irrespective of the SWR origin laterality (*SI Appendix*, Fig. S2 *B* and *C*). Higher presence of HFA modulation in temporal cortex and amygdala could reflect enhanced connectivity between the hippocampus and temporal lobe structures relative to hippocampal–frontal connectivity, although the frontal cortex is one of the principal hippocampal target areas outside the temporal lobe (40). While it is possible that some instances of hippocampal SWRs in the present study coincide with previously reported extrahippocampal SWRs (20, 41), we quantified the extrahippocampal peri-SWR HFA modulation regardless of the presence or absence of local SWRs.

SWR–SWA and SWR–SP Phase Locking Are Associated with Local HFA Modulation. We demonstrate that the consistent relation between the hippocampal SWR timing and subcortical/cortical oscillatory phases (SWR–SWA and SWR–SP phase locking) strongly predicts a subset of local populations participating in global peri-SWR activation (32), proposed to be involved in memory consolidation (35, 37). In addition, hippocampal SWRs are phase locked to local hippocampal SWA- and SP-frequency oscillations (*SI Appendix*, Fig. S4*B*), which in turn show phase synchrony with extrahippocampal SWR–SWA+ or SWR–SP+ target sites. Therefore,

a hippocampal–extrahippocampal phase synchrony might be a necessary prerequisite for SWR phase locking to extrahippocampal oscillations. The sites with significant peri-SWR modulation or no modulation coexist in the same brain structures (Fig. 2*A*). Such a selective pattern of peri-SWR HFA modulation suggests that besides the necessary anatomical connectivity, the local subcortical/cortical SWA and SP could provide a gating mechanism that enables the peri-SWR HFA modulation. Interestingly, the regional distributions of SWR locking phases were significantly different between the target sites in the amygdala, temporal, and frontal cortex, ipsilateral to SWR location (*SI Appendix*, Fig. S4*A*). This does not appear to reflect the different dipole orientations (*SI Appendix*, Fig. S4*A*). Rather, it could be reflecting the consistent SWA trajectory prior to reaching the hippocampus and triggering the SWR (18). The traveling SWA tend to emerge from frontal lobe and spread in the anterior–posterior direction (23), but the site of origin, traveling directions, and velocities across individual waves are highly variable (22, 23). Moreover, ∼85% of SWA in the human brain shows relatively limited extent, invading less than one-half of recorded locations (22). Although the SWA trajectories are constrained by anatomical connections (42), SWA is theoretically capable of sampling from a large combinatorial space of subcortical/cortical populations, enabling their synchronous activity during individual peri-SWR windows. SWA is regulated by local learning history and appears with higher amplitude and more often in the regions involved in recent learning (43, 44). These results also suggest that SP, frequently nested in SWA (20, 45), represent an additional oscillatory mechanism for selective activation of extrahippocampal populations during SWRs. However, although the SWR–SP phase locking shows even stronger preference for HFA+ target sites than SWR–SWA phase locking (10-fold versus 3 to 4-fold; *SI Appendix*, Fig. S3*A*), SWR–SP phase locking was almost completely absent in the hemisphere contralateral to SWR location. This might suggest a limited spatial extent of SP-associated synchronization of extrahippocampal areas with hippocampus during SWR windows.

SWA Phase and SWR Amplitude Predict Cortico–Cortical Functional Coupling. SWA synchronization in anatomically distributed neuronal populations during peri-SWR periods could facilitate formation of transient neuronal coalitions providing a mechanism for binding of distributed memory traces (35). We demonstrate that the presence of long-distance interactions in the fronto–temporal network during SWR windows is predictable based on the phase differences between local SWA. Critically, this correlation is present after factoring out the common coupling to global brain activity by applying a GLM. This is a widely used approach for quantifying the relative contributions of multiple predictors on the activity of single neurons and neuronal populations (46). The relation between the oscillatory phase offset and functional connectivity strength between the different local populations has been previously demonstrated in the visual cortex (34). The association between the pairwise local SWA phase differences and HFA coupling could emerge if the SWA events follow a relatively consistent cortical trajectory prior to invading the hippocampus, biasing the emergence of SWR (18). This could result in a repetitive stable cortico–cortical and hippocampo–cortical phase alignment during SWR events. Next, the local SWA phase–dependent excitability states could determine the interaction between the pairs of target sites coactive during SWR. In addition, the presence of cortico–cortical coupling is predictable based on the current SWR amplitude. As the larger-amplitude SWRs are associated with the recruitment of a more widespread hippocampal population (36), the association between the cortico–cortical coupling and SWR amplitude could reflect the stronger hippocampal output to distributed cortical networks. Alternatively, if the cortical input to hippocampus is stronger due to a strong cortical synchrony, it might result in a

Skelin et al.
Coupling between slow waves and sharp-wave ripples engages distributed neural activity during sleep in humans

PNAS | 7 of 10
https://doi.org/10.1073/pnas.2012075118

stronger hippocampal recruitment and a larger SWR amplitude. The observed dynamics suggest the role of SWA phase–organized distributed neuronal coalitions in hippocampal-dependent memory consolidation, supporting binding of distributed memory traces (3). It should be noted that this study has not directly analyzed memory consolidation dynamics, but its interpretation relies on the extensive literature associating the SWRs, SWA, and SP or their temporal alignment with the efficiency of sleep-dependent memory consolidation (13, 16, 47). In addition, future studies could address the role of oscillations <0.5 Hz—strongly implicated in hippocampal–cortical dynamics (19, 45)—in large-scale coupling of distributed neuronal populations, especially in the context of SWR windows.

Summary. Various models of hippocampal-dependent memory consolidation implicate binding between the hippocampal memory traces reactivated during SWRs and the subcortical/cortical populations encoding various aspects of the same experience (2, 3). These results suggest the critical role of a consistent phase relation between the hippocampal SWRs and subcortical/cortical SWA and SP for the selection of local populations active during SWR windows. In addition, the local SWA phases during SWRs and SWR amplitudes predict the functional coupling between the distant cortical populations, enabling the plasticity necessary for binding of distributed memory traces. Our findings implicate SWR–SWA interplay as a potential mechanism affecting the content, fidelity, and strength of consolidated memories.

Methods

Participants. A total of 12 pharmacoresistant epileptic patients (7 males and 5 females, age 38 ± 4 [mean ± SEM], range 24 to 57) undergoing presurgical evaluation of seizure foci at the University of California, Irvine (UCI) Medical Center were included in the study based on written informed consent. This study was approved by the UCI Institutional Review Board. The subjects were stereotactically implanted with 6 to 10 intracranial depth electrodes (Integra or Ad-Tech, 8 to 10 macroelectrodes with 5-mm interelectrode spacing) under robotic assistance (Rosa Surgical Robot, Medtech). Electrode placements were driven strictly by clinical diagnostic needs and included the unilateral or bilateral implants in the hippocampus, amygdala, temporal, and frontal cortices. Details of individual patient electrode locations are given in the *SI Appendix,* Table S1. The criteria for subject inclusion were as follows: 1) presence of at least one hippocampal electrode with >100 SWRs recorded during the seizure-free overnight sleep and 2) presence of electrodes in at least one extrahippocampal region (amygdala, temporal, or frontal cortices).

Electrode Localization. Electrode localization was done using the preimplantation MRI and postimplantation computed tomography (CT) images. Both images were transformed into Talairach space, followed by MRI segmentation (Freesurfer 5.3.067) and coregistration of T1-weighted structural MRI scans to the CT (48). The electrode locations and selection of white matter contacts for rereferencing was verified by the epileptologist (J.J.L.).

Recording Locations. We analyzed SWRs recorded on 32 hippocampal locations (20 in left and 12 in right hemisphere; Fig. 1*C*). The extrahippocampal recording sites were grouped in three regions (Fig. 1*B*): amygdala (including the basolateral, lateral, and centromedial amygdala), temporal (including the insula, entorhinal, parahippocampal, inferior, medial, and superior temporal cortices), and frontal cortex (including the orbitofrontal, medial prefrontal, dorsomedial, and cingulate cortices). Regional distribution of extrahippocampal recording sites included are as follows: 36 (19 left, 17 right) in amygdala, 180 (106 left, 74 right) in temporal, and 189 (89 left, 100 right) in frontal cortex (Fig. 1*B* and *SI Appendix,* Table S1). Distribution of recording sites at individual subject, hemispheric, and regional levels are shown in *SI Appendix,* Table S1.

Experimental Design. The iEEG signals were recorded during overnight sleep, typically starting at 8:00 to 10:00 PM and lasting ~8 to 12 h. A single overnight sleep recording was used from each participant. The iEEG was analog filtered with 0.01 Hz high-pass cutoff and recorded at 5,000 Hz using the Nihon Kohden recording system (256-channel amplifier, model JE120A) or at 8,000 Hz using the Neuralynx ATLAS clinical system. Sleep staging was performed in 30-s blocks by a sleep specialist (B.A.M.) based on the visual inspection of scalp EEG at frontal, central, and occipital derivations and electrooculogram and electromyogram,

guided by standard criteria (14, 27). The NREM sleep stages 2 to 4 were used in further analysis (Fig. 1*D*).

Data Preprocessing. Recordings were rereferenced to the nearest white matter contact, resampled to 2,000 Hz with linear interpolation (resample.m function in Matlab Signal Processing Toolbox), and high-pass filtered at 0.5 Hz using fourth order Chebyshev filter. The data analysis and visualization was performed using the custom-written Matlab code, as well as the Freely Moving Animal (FMA; fmatoolbox.sourceforge.net/), Circular Statistics (49), and FieldTrip (48, 50) toolboxes.

Electrodes outside of the primary epileptogenic regions were used in the analysis. Furthermore, IEDs on those electrodes were detected based on the combination of amplitude and derivative thresholds (19). For amplitude-based IED detection, each iEEG trace was low-pass filtered (300-Hz cutoff frequency) and the envelope of filtered trace was z-scored, while for the derivative-based IED detection, absolute differences between the consecutive voltage samples were z-scored. IEDs were detected based on the threshold crossing (mean + 5 SD) by either the amplitude or derivative trace (*SI Appendix,* Fig. S1*A*). This method is optimized for detection of sharp transients that correspond to IEDs. Finally, automatic IED detection accuracy was validated by comparison with visual scoring performed by an epileptologist (*SI Appendix,* Fig. S1*B*).

SWR Detection. Following electrode localization, iEEG from hippocampal channels was bandpass filtered in SWR range (80 to 150 Hz) using the fourth order Chebyshev filter (filtfilt.m function in Matlab Signal Processing Toolbox), rectified, and the upper envelope of rectified trace was z-scored. SWRs were detected using the FMA Toolbox based on the double-threshold–crossing criteria: 1) envelope trace exceeding mean + 2 SDs for 20 to 100 ms and 2) the peak during this period exceeding mean + 5 SDs (Fig. 1*E*). SWRs within 1 s from nearest IED and hippocampal channels with <100 SWRs remaining after exclusion of SWRs in IED proximity were excluded from analysis.

Analysis Approach. The analysis was done using all the hippocampal channels that passed the inclusion criteria. This approach was chosen because the SWRs at different hippocampal locations might be associated with different dynamics in the same extrahippocampal populations. In addition, including the hippocampal channels from both hemispheres allowed the testing of both ipsi- and contralateral brain dynamics during peri-SWR periods. Therefore, the peri-SWR dynamics in all of the extrahippocampal recording sites were analyzed relative to SWRs on each individual different hippocampal site in the same subject. For the purpose of this analytical approach, each extrahippocampal recording site was defined as a target site, with respect to individual hippocampal site. Target sites in each region were classified as ipsi- or contralateral relative to SWR location. The regional distribution of target sites included: 87 (44 ipsilateral, 43 contralateral) in the amygdala, 521 (250 ipsilateral, 271 contralateral) in temporal, and 700 (331 ipsilateral, 369 contralateral) in frontal cortex.

All the corrections for multiple comparisons were done using the Benjamini–Hochberg method (51). Correction factor was based on the number of recording locations in individual patients for the peri-SWR HFA modulation or the number of regional and hemispheric comparisons in other cases. Analysis was performed on all the target sites that passed inclusion criteria for a given analysis. Specifically, the target sites with at least 50 IED-free peri-SWR windows (±1 s) were used for peri-SWR HFA modulation (Fig. 2 and *SI Appendix,* Fig. S2), SWR–SWA or SWR–SP phase locking (Fig. 3 and *SI Appendix,* Fig. S3), and phase synchrony with hippocampus. The target sites used for HFA pairwise coupling analysis were selected based on two additional criteria: 1) significant peri-SWR HFA modulation and 2) significant SWR–SWA phase locking (Fig. 4). Hemispheric and regional comparisons of HFA+, SWA–SWR, and SWR–SP phase locking percentages were done using the linear mixed-effects model, with regional or hemispheric labels as fixed effect predictors and subject identities as random effect predictors (*SI Appendix,* Fig. S2). Phase locking was considered significant if the real PLV exceeded 98% of null distribution PLV (Fig. 3 and *SI Appendix,* Figs. S3 and S4). Comparisons between the extrahippocampal-coupling prediction model performances were done using the linear mixed-effects model, with the model identities as fixed effect predictors and subject identities as random effect predictors.

Peri-SWR HFA Modulation. The HFA analytical amplitude was calculated by bandpass filtering the raw iEEG in 70 to 200 Hz range, Hilbert transforming the filtered signal (hilbert.m function in Matlab Signal Processing Toolbox), and extracting the analytic signal amplitude. HFA amplitude trace was smoothed by convolving with Gaussian kernel (15-ms width, fastsmooth.m function in Matlab Signal Processing Toolbox) and binned (25-ms bin size), resulting in 20 time bins extending over the ±250-ms window centered at SWR peak (peri-SWR window).

The time window between −500 and −250 ms relative to SWR peak was used as a baseline (Fig. 2B). The choice of baseline was motivated by the following criteria: 1) relatively stable HFA activity (Fig. 2B); 2) proximity to SWR event, minimizing the effects of HFA fluctuations across the sleep stages or NREM episodes (52, 53); and 3) consistent temporal relation to SWR event.

Baseline normalization was done at single-trial level by z-scoring concatenated baseline and peri-SWR HFA time windows. Peri-SWR HFA modulation was assessed at individual time bin level by comparing the mean HFA within each bin with the mean HFA from the baseline period using the two-tailed paired Student's t test ($P < 0.05$). Correction for multiple comparisons was done using Benjamini–Hochberg method (51) based on the number of simultaneously recorded extrahippocampal electrodes in a given subject. In addition, peri-SWR HFA modulation significance criteria at individual-channel level included the presence of at least two consecutive time bins (a total of 50 ms) showing significant peri-SWR HFA modulation in the same direction. Target sites were first classified based on the presence (HFA+) or absence (HFA−) of significant peri-SWR HFA modulation. Based on the peri-SWR HFA modulation type, HFA+ sites were further classified as positively, negatively, or mixed modulated, the latter defined by the presence of both positive and negative modulation periods during peri-SWR window (Fig. 2B). The time-bin width choice (25 ms) was based on the fine temporal structure of peri-SWR cortical neuronal spiking fluctuations in rodents (6) and humans (22). While the HFA shows a high correlation with the multiunit activity (26, 54), a sum of all the spikes in the vicinity of the electrode, it does not positively or linearly correlate with each individual spike train (55). Therefore, we are interpreting HFA as an indirect measure of the adjacent population spiking activity, without implying correlation with the activity of individual single neurons.

Phase-Locking and Synchrony Analysis. The raw iEEG recorded at each extrahippocampal location was bandpass filtered in the SWA (0.5 to 4 Hz) or SP range (7 to 15 Hz). Filtered traces were Hilbert transformed, and instantaneous phases were extracted using the angle.m function in Matlab. SWR phase locking to SWA or SP frequency range is defined as a measure of consistency of hippocampal or subcortical/cortical SWA/SP phase at the times of hippocampal SWR peaks (Fig. 3B). Phase-locking was quantified using the PLV method (33):

$$\text{PLV} = \frac{1}{N} \left| \sum_{n=1}^{N} \exp(j\theta(tSWR, n)) \right|.$$

For the PLV calculation, $\theta(tSWR, n)$ is defined as the SWA/SP phase, or hippocampal target site phase difference, at the peak of the nth SWR event. PLV values range between 0 and 1, with higher values reflecting the narrower phase distribution. PLV null distribution was generated by randomly jittering the SWR peak times within ±1,000-ms window and obtaining the SWA/SP phases from those timepoints. Shuffling was performed 1,000 times, and the PLV was considered significant if the real PLV exceeded 98% of PLV null distribution. For each hippocampal or target site channel showing SWR–SWA or SWR–SP phase locking, mean SWR–SWA or SWR–SP phase angle was computed using circ_mean.m function [Matlab Circular Statistics Toolbox (49)]. In addition, significant phase preference of overall and regional SWR–SWA or SP locking-phase distributions (SI Appendix, Fig. S4) was assessed by calculating the subject-average SWR–SWA or SWR–SP PLV and comparing it to the null distribution, generated from the 1,000 random phase sets of equal sample size. For the comparison of regional locking-phase distributions (SI Appendix, Fig. S4), locking phases were converted into a scalar by rotating the circular plane with the angle identified by fixed effect coefficients obtained from fitting multiple regression models. Finally, the resulting scalars were used as dependent variables in a linear mixed-effects model, with the region as fixed effect predictor and subject identity as a random effect predictor ($P < 0.05$, Benjamini–Hochberg correction for multiple comparisons based on the number of regional comparisons). The SWR–SWA or SWR–SP PLV comparisons were performed using the linear mixed model, with the presence or absence of peri-SWR HFA modulation (HFA+ or HFA−) as a fixed variable and subject identity as an independent variable (Fig. 3D and SI Appendix, Fig. S3E; $P < 0.05$).

To verify that SWR–SWA or SWR–SP phase locking is not driven by higher SWA or SP amplitude on a given target site; iEEG signal from each target site was filtered in SWA (0.5 to 4 Hz) or SP (7 to 15 Hz) range, and the target site average amplitude of each frequency range was computed as the mean of analytical amplitude from individual peri-SWR windows, defined as the absolute value of the Hilbert-transformed trace. Comparison of peri-SWR SWA or SP amplitude between the SWR–SWA+ or SP+ and SWR–SWA− or SP− target sites was done using the linear mixed-effects model, with the presence or absence of phase locking as a fixed effect predictor and subject identity as a random effect predictor ($P < 0.05$; SI Appendix, Fig. S3B). The lack of significant group difference in peri-SWR SWA or SP amplitude was interpreted as ruling

out the possibility of peri-SWR amplitude having a confounding effect on the phase extraction and phase-locking calculation. Joint peri-SWR time histogram (JPSTH) for individual target sites was obtained by binning the SWA and HFA amplitude during the ±500-ms window around each individual SWR event (25-ms time bins), z-scoring each binned trace, and computing the outer product of the HFA and SWA trace vectors. Resulting JPSTHs were averaged across all the SWR events at the individual target site. Finally, the subject averages and grand averages were obtained separately for SWR–SWA+ and SWR–SWA− target sites (Fig. 3A).

Analysis of Extrahippocampal Pairwise Coupling during SWR Windows. Extrahippocampal pairwise coupling during SWR windows was estimated using the peri-SWR HFA time courses from the pairs of simultaneously recorded target sites showing both significant peri-SWR HFA modulation and significant SWR–SWA phase locking. The analysis included the interregional pairs from the regions that contained eligible target site pairs in at least four subjects (amygdala–temporal and frontal–temporal pairs). To prevent the influence of absolute HFA levels on the resulting coupling estimates, individual peri-SWR HFA time courses were z-scored. All the analysis was performed at the individual SWR-window level using the two different approaches, Pearson correlation, and GLM. The r_{ABn} coupling coefficient was defined as the Pearson correlation between the peri-SWR HFA time courses on the pair of simultaneously recorded target sites during the nth SWR window (HFA-A_n and HFA-B_n). The GLM analysis was performed by modeling the HFA-A_n as a function of HFA time course of another target site (HFA-B_n) and averaged population peri-SWR HFA time course (HFA-pop_n), both from the same trial. Population was defined as all the simultaneously recorded target sites, except A and B. All of the analysis was done at zero time lag. The model fitting was done using a Matlab glmfit.m function with normal distribution. For each target site pair (A, B) and individual SWR event (SWR$_n$), the model produced two coefficients (β_{ABn} and β_{popABn}), reflecting the predictive power of HFA-A_n and HFA-$popAB_n$ on HFA-B_n. For each target site pair, the absolute SWR–SWA phase difference during the SWR$_n$ event (Φdiff_n) was computed as follows:

$$\Phi\text{diff}_n = |\Phi_{An} - \Phi_{Bn}|,$$

with Φ_{An} and Φ_{Bn} representing the local SWA phases on the sites A and B, coinciding with the SWR$_n$ peak. SWR amplitude was defined as the peak z-scored value of the SWR frequency range envelope during SWR$_n$ (SWRamp$_n$). The null distribution of coupling coefficients for a given target site pair/SWR window was constructed by estimating the coupling between the HFA-A and HFA-B from different, randomly selected SWR windows (100 shuffling iterations). Coupling significance was determined based on the percentile of real coupling coefficient (β_{ABn} or r_{ABn}) relative to the null distribution (<2.5 and >97.5 percentiles representing the significance thresholds). Next, each subject dataset was divided into a training and testing set (ratio 3:1), and the SVM with a linear kernel was trained to classify individual target site pairs during a given SWR window as either coupled or uncoupled (responder category). Separate models were trained for predicting the β_{ABn} or r_{ABn} coupling. The hyperparameters of the models were determined with the minimal 10-fold cross-validation loss with the training data (function fitcecoc.m in Matlab). The model performance was evaluated (function predict.m in Matlab) using the predictors from the testing data (Φdiff_n, SWRamp$_n$, or both) and comparing the model outputs (coupled/uncoupled) with the ground truth. The same procedure was repeated separately in each subject for 100 classifier iterations, each time with different training and testing samples. The model prediction accuracy was expressed as the percentage of correct predictions (coupled or uncoupled) from a given model iteration. The subject-level model performances were further evaluated by plotting the receiver operating characteristic curves. Between-model comparisons were performed using the linear mixed-effects model, with the prediction accuracy as a response variable, model identity as a fixed effect predictor variable, and subject identity as a random effect predictor variable ($P < 0.05$, with the Benjamini–Hochberg method for multiple comparison correction based on the number of model comparisons).

Skelin et al.
Coupling between slow waves and sharp-wave ripples engages distributed neural activity during sleep in humans

PNAS | 9 of 10
https://doi.org/10.1073/pnas.2012075118

NEUROSCIENCE

1. L. R. Squire, P. Alvarez, Retrograde amnesia and memory consolidation: A neurobiological perspective. *Curr. Opin. Neurobiol.* **5**, 169–177 (1995).
2. L. Nadel, M. Moscovitch, Memory consolidation, retrograde amnesia and the hippocampal complex. *Curr. Opin. Neurobiol.* **7**, 217–227 (1997).
3. G. Buzsáki, Two-stage model of memory trace formation: A role for "noisy" brain states. *Neuroscience* **31**, 551–570 (1989).
4. M. A. Wilson, B. L. McNaughton, Reactivation of hippocampal ensemble memories during sleep. *Science* **265**, 676–679 (1994).
5. K. Diba, G. Buzsáki, Forward and reverse hippocampal place-cell sequences during ripples. *Nat. Neurosci.* **10**, 1241–1242 (2007).
6. A. Peyrache, M. Khamassi, K. Benchenane, S. I. Wiener, F. P. Battaglia, Replay of rule-learning related neural patterns in the prefrontal cortex during sleep. *Nat. Neurosci.* **12**, 919–926 (2009).
7. A. A. Wilber, I. Skelin, W. Wu, B. L. McNaughton, Laminar organization of encoding and memory reactivation in the parietal cortex. *Neuron* **95**, 1406–1419.e5 (2017).
8. P. Fries, A mechanism for cognitive dynamics: Neuronal communication through neuronal coherence. *Trends Cogn. Sci.* **9**, 474–480 (2005).
9. G. Buzsáki, Hippocampal sharp wave-ripple: A cognitive biomarker for episodic memory and planning. *Hippocampus* **25**, 1073–1188 (2015).
10. H. S. Kudrimoti, C. A. Barnes, B. L. McNaughton, Reactivation of hippocampal cell assemblies: Effects of behavioral state, experience, and EEG dynamics. *J. Neurosci.* **19**, 4090–4101 (1999).
11. C. S. Lansink, P. M. Goltstein, J. V. Lankelma, B. L. McNaughton, C. M. Pennartz, Hippocampus leads ventral striatum in replay of place-reward information. *PLoS Biol.* **7**, e1000173 (2009).
12. A. G. Siapas, M. A. Wilson, Coordinated interactions between hippocampal ripples and cortical spindles during slow-wave sleep. *Neuron* **21**, 1123–1128 (1998).
13. N. Maingret, G. Girardeau, R. Todorova, M. Goutierre, M. Zugaro, Hippocampo-cortical coupling mediates memory consolidation during sleep. *Nat. Neurosci.* **19**, 959–964 (2016).
14. R. F. Helfrich *et al.*, Bidirectional prefrontal-hippocampal dynamics organize information transfer during sleep in humans. *Nat. Commun.* **10**, 3572 (2019).
15. A. Sirota, J. Csicsvari, D. Buhl, G. Buzsáki, Communication between neocortex and hippocampus during sleep in rodents. *Proc. Natl. Acad. Sci. U.S.A.* **100**, 2065–2069 (2003).
16. G. Girardeau, K. Benchenane, S. I. Wiener, G. Buzsáki, M. B. Zugaro, Selective suppression of hippocampal ripples impairs spatial memory. *Nat. Neurosci.* **12**, 1222–1223 (2009).
17. A. Fernández-Ruiz *et al.*, Long-duration hippocampal sharp wave ripples improve memory. *Science* **364**, 1082–1086 (2019).
18. Y. Isomura *et al.*, Integration and segregation of activity in entorhinal-hippocampal subregions by neocortical slow oscillations. *Neuron* **52**, 871–882 (2006).
19. B. P. Staresina *et al.*, Hierarchical nesting of slow oscillations, spindles and ripples in the human hippocampus during sleep. *Nat. Neurosci.* **18**, 1679–1686 (2015).
20. Z. Clemens *et al.*, Temporal coupling of parahippocampal ripples, sleep spindles and slow oscillations in humans. *Brain* **130**, 2868–2878 (2007).
21. M. Steriade, D. Contreras, R. Curró Dossi, A. Nuñez, The slow (< 1 Hz) oscillation in reticular thalamic and thalamocortical neurons: Scenario of sleep rhythm generation in interacting thalamic and neocortical networks. *J. Neurosci.* **13**, 3284–3299 (1993).
22. Y. Nir *et al.*, Regional slow waves and spindles in human sleep. *Neuron* **70**, 153–169 (2011).
23. M. Massimini, R. Huber, F. Ferrarelli, S. Hill, G. Tononi, The sleep slow oscillation as a traveling wave. *J. Neurosci.* **24**, 6862–6870 (2004).
24. M. H. Mohajerani, D. A. McVea, M. Fingas, T. H. Murphy, Mirrored bilateral slow-wave cortical activity within local circuits revealed by fast bihemispheric voltage-sensitive dye imaging in anesthetized and awake mice. *J. Neurosci.* **30**, 3745–3751 (2010).
25. K. G. Phillips *et al.*, Decoupling of sleep-dependent cortical and hippocampal interactions in a neurodevelopmental model of schizophrenia. *Neuron* **76**, 526–533 (2012).
26. S. Ray, J. H. Maunsell, Different origins of gamma rhythm and high-gamma activity in macaque visual cortex. *PLoS Biol.* **9**, e1000610 (2011).
27. A. Rechtschaffen, A. Kales, *A Manual of Standardized Terminology, Techniques and Scoring System for Sleep Stages of Human Subjects* (US Dept. of Health, Education, and Welfare, Bethesda, MD, 1968).
28. S. Redline *et al.*, The effects of age, sex, ethnicity, and sleep-disordered breathing on sleep architecture. *Arch. Intern. Med.* **164**, 406–418 (2004).
29. M. Le Van Quyen *et al.*, Cell type-specific firing during ripple oscillations in the hippocampal formation of humans. *J. Neurosci.* **28**, 6104–6110 (2008).
30. A. Bragin, J. Engel Jr, C. L. Wilson, I. Fried, G. Buzsáki, High-frequency oscillations in human brain. *Hippocampus* **9**, 137–142 (1999).
31. W. E. Skaggs *et al.*, EEG sharp waves and sparse ensemble unit activity in the macaque hippocampus. *J. Neurophysiol.* **98**, 898–910 (2007).
32. N. K. Logothetis *et al.*, Hippocampal-cortical interaction during periods of subcortical silence. *Nature* **491**, 547–553 (2012).
33. J. P. Lachaux, E. Rodriguez, J. Martinerie, F. J. Varela, Measuring phase synchrony in brain signals. *Hum. Brain Mapp.* **8**, 194–208 (1999).
34. T. Womelsdorf *et al.*, Modulation of neuronal interactions through neuronal synchronization. *Science* **316**, 1609–1612 (2007).
35. G. Buzsáki, A. Draguhn, Neuronal oscillations in cortical networks. *Science* **304**, 1926–1929 (2004).
36. J. Patel, E. W. Schomburg, A. Berényi, S. Fujisawa, G. Buzsáki, Local generation and propagation of ripples along the septotemporal axis of the hippocampus. *J. Neurosci.* **33**, 17029–17041 (2013).
37. I. Skelin, S. Kilianski, B. L. McNaughton, Hippocampal coupling with cortical and subcortical structures in the context of memory consolidation. *Neurobiol. Learn. Mem.* **160**, 21–31 (2019).
38. T. J. Teyler, P. DiScenna, The hippocampal memory indexing theory. *Behav. Neurosci.* **100**, 147–154 (1986).
39. A. Peyrache, F. P. Battaglia, A. Destexhe, Inhibition recruitment in prefrontal cortex during sleep spindles and gating of hippocampal inputs. *Proc. Natl. Acad. Sci. U.S.A.* **108**, 17207–17212 (2011).
40. E. L. Johnson *et al.*, Dynamic frontotemporal systems process space and time in working memory. *PLoS Biol.* **16**, e2004274 (2018).
41. A. P. Vaz, S. K. Inati, N. Brunel, K. A. Zaghloul, Coupled ripple oscillations between the medial temporal lobe and neocortex retrieve human memory. *Science* **363**, 975–978 (2019).
42. M. Murphy *et al.*, Source modeling sleep slow waves. *Proc. Natl. Acad. Sci. U.S.A.* **106**, 1608–1613 (2009).
43. R. Huber, M. F. Ghilardi, M. Massimini, G. Tononi, Local sleep and learning. *Nature* **430**, 78–81 (2004).
44. R. Huber *et al.*, Arm immobilization causes cortical plastic changes and locally decreases sleep slow wave activity. *Nat. Neurosci.* **9**, 1169–1176 (2006).
45. J. G. Klinzing *et al.*, Spindle activity phase-locked to sleep slow oscillations. *Neuroimage* **134**, 607–616 (2016).
46. P.-J. Lahaye, J.-B. Poline, G. Flandin, S. Dodel, L. Garnero, Functional connectivity: Studying nonlinear, delayed interactions between BOLD signals. *Neuroimage* **20**, 962–974 (2003).
47. S. Gais, M. Mölle, K. Helms, J. Born, Learning-dependent increases in sleep spindle density. *J. Neurosci.* **22**, 6830–6834 (2002).
48. A. Stolk *et al.*, Integrated analysis of anatomical and electrophysiological human intracranial data. *Nat. Protoc.* **13**, 1699–1723 (2018).
49. P. Berens, CircStat: A MATLAB toolbox for circular statistics. *J. Stat. Softw.* **31**, 1–21 (2009).
50. R. Oostenveld, P. Fries, E. Maris, J.-M. Schoffelen, FieldTrip: Open source software for advanced analysis of MEG, EEG, and invasive electrophysiological data. *Comput. Intell. Neurosci.* **2011**, 156869 (2011).
51. Y. Benjamini, Y. Hochberg, Controlling the false discovery rate: A practical and powerful approach to multiple testing. *J. R. Stat. Soc. B* **57**, 289–300 (1995).
52. V. V. Vyazovskiy *et al.*, Cortical firing and sleep homeostasis. *Neuron* **63**, 865–878 (2009).
53. A. D. Grosmark, K. Mizuseki, E. Pastalkova, K. Diba, G. Buzsáki, REM sleep reorganizes hippocampal excitability. *Neuron* **75**, 1001–1007 (2012).
54. R. Mukamel *et al.*, Coupling between neuronal firing, field potentials, and FMRI in human auditory cortex. *Science* **309**, 951–954 (2005).
55. J. R. Manning, J. Jacobs, I. Fried, M. J. Kahana, Broadband shifts in local field potential power spectra are correlated with single-neuron spiking in humans. *J. Neurosci.* **29**, 13613–13620 (2009).
56. I. Skelin, HumanRippleProject. GitHub. https://github.com/IvanSkelinM/HumanRippleProject. Deposited 12 November 2020.